

THE STRUCTURE OF THE PROTOTYPE BIPOLAR PROTOPLANETARY NEBULA CRL 2688 (EGG NEBULA):
BROADBAND, POLARIMETRIC, AND H₂ LINE IMAGING WITH NICMOS ON THE *HUBBLE SPACE TELESCOPE*

RAGHVENDRA SAHAI,¹ DEAN C. HINES,² JOEL H. KASTNER,³ DAVID A. WEINTRAUB,⁴ JOHN T. TRAUGER,¹
MARCIA J. RIEKE,² RODGER I. THOMPSON,² AND GLENN SCHNEIDER²
Received 1997 August 6; accepted 1997 October 30; published 1997 December 30

ABSTRACT

High-resolution near-infrared (1.65–2.1 μm) images and 2 μm polarimetric images of the inner 19".5 \times 19".3 region of the bipolar protoplanetary nebula CRL 2688, taken with the newly installed Near-Infrared Camera and Multiobject Spectrometer (NICMOS) aboard the *Hubble Space Telescope* (*HST*), are reported. The NICMOS images reveal a wealth of structure also seen in *HST* Wide Field Planetary Camera 2 images but not detected in previous, ground-based near-infrared imaging studies. In particular, we detect a system of concentric arcs centered on, and twin “searchlight beams” emanating from, the obscured central star. The images also show two sharply bounded spindle-shaped polar cavities with point-symmetric structure, and the 2.122 μm H₂ S(1) $v = 1-0$ emission-line image clearly resolves the sharp interface between the high-velocity outflow that produces these polar cavities and the surrounding slow outflow that forms the extended nebula. The H₂ image also resolves the bright equatorial H₂ emission into distinct components and elucidates their detailed morphologies. We have discovered, within the dark lane that bifurcates the bipolar lobes of CRL 2688, a compact source of unpolarized light. Our imaging polarimetry shows that this source is not the post-asymptotic giant branch star that illuminates the nebula; we conclude that the compact source is a companion star.

Subject headings: ISM: reflection nebulae — stars: AGB and post-AGB — stars: circumstellar matter — stars: individual (CRL 2688) — stars: mass loss — techniques: polarimetric

1. INTRODUCTION

CRL 2688 (also known as the Egg Nebula) is a bipolar reflection nebula illuminated by a post-asymptotic giant branch (AGB) star. First observed on the Palomar Observatory Sky Survey (Ney et al. 1975) and located at an estimated distance of 1 kpc, it is the most prominent and well studied (see, e.g., Latter et al. 1993; Young et al. 1992; Yamamura et al. 1995; Knapp et al. 1994; Cox et al. 1997) member of the class of protoplanetary nebulae (PPN)—objects in a short-lived transition phase between the AGB and planetary nebula evolutionary phases of 1–8 M_{\odot} mass stars. Recently, Sahai et al. (1998, hereafter STWS98) obtained a high-resolution (0".1) image of CRL 2688 with the Wide Field Planetary Camera 2 (WFPC2) on the *Hubble Space Telescope* (*HST*) that shows a double pair of radial searchlight-beam features emanating from, and a large number of roughly concentric arcs around, the nebular center. According to a long-held model of CRL 2688 based on imaging from the ground (see, e.g., Morris 1981; Yusef-Zadeh, Morris, & White 1984; Latter et al. 1993), the nebular morphology results from a density distribution that decreases monotonically from the equator toward the polar axis (defined as the nebular major axis), dropping sharply to zero at a latitude of $\approx 83^{\circ}$. On the basis of the WFPC2 images, however, STWS98 conclude that the morphology of CRL 2688 is best understood in terms of a flattened optically thick dust

cocoon with a pair of annular-shaped polar cavities surrounding the central star (see Fig. 5 of STWS98). Starlight escaping through these cavities and scattered into the line of sight by dust in an extended round nebula surrounding the cocoon produces the searchlight-beam features. An earlier ground-based near-IR study of CRL 2688 by Latter et al. (1993) revealed that the morphology of the *K*-band continuum is similar to that seen at shorter wavelengths (*V* and *I*) but is quite different from that of the 2.122 μm H₂ S(1) $v = 1-0$ emission (which arises from shocked gas) that has a remarkable quadrupolar appearance, comprised of polar and equatorial components (Gatley, Depoy, & Fowler 1988). The origin of the equatorial component is a puzzle, and the limited ground-based spatial resolution has been an impediment to solving this puzzle.

Noting the important advantage afforded by *HST*'s high-resolution in understanding the structure of CRL 2688, we have obtained near-IR images of this PPN with the Near-Infrared Camera and Multiobject Spectrometer (NICMOS), recently installed on the *HST*. Our aim is to probe material in the dust cocoon hidden from view in the WFPC2 image because of high extinction, elucidate the nature and origin of the H₂ S(1) line emission, and use polarimetry to constrain the location and number of illuminating sources. In this Letter we present the results of our observations and discuss briefly preliminary conclusions about the structure of CRL 2688 that are relevant to the issue of how some AGB stars evolve into bipolar PPN and, eventually, ringlike and butterfly planetary nebulae.

2. OBSERVATIONS

CRL 2688 was imaged through several filters with camera 2 (NIC2) of NICMOS, which has a field of view of 19".5 \times 19".3 and a plate scale of 0".076 pixel⁻¹ (Thompson et al. 1998).

¹ Jet Propulsion Laboratory, MS 183-900, California Institute of Technology, Pasadena, CA 91109.

² Steward Observatory, University of Arizona, Tucson, AZ 85721.

³ Center for Space Research, Massachusetts Institute of Technology, Building 37-667a, Cambridge, MA 02139.

⁴ Department of Physics and Astronomy, Vanderbilt University, P.O. Box 1807, Station B, Nashville, TN 37235.

The observations are summarized in Table 1. For each filter, a four-step spiral dither was used with nonintegral (20.5) pixel offsets to better sample the point-spread function and remove bad pixels and other artifacts. The images were reduced with CALNICA in the STSDAS package of IRAF. Residual artifacts are caused by (1) preflight thermal vacuum flats that were required for some filters that did not yet have on-orbit flat fields and (2) the “pedestal effect” associated with dark frame subtraction (Thompson et al. 1998).

Figure 1 (Plate L44) shows a color composite of the NICMOS continuum-subtracted $H_2 S(1)$ (red) and F165M (green) images, together with the WFPC2 (blue) image (from STWS98). Each of the individual images in Figure 1 are shown separately in Figure 2 (Plate L45, panels *a–c*). The sharp structures in each image in Figure 1 have been modestly enhanced. Two bright spindle-like bubbles can be seen in the infrared, aligned precisely along the polar axis (P.A. = 19°) of the nebula, in the middle of the extended searchlight beams seen in the WFPC2 image. The NICMOS H_2 image resolves the bright equatorial emission into distinct components and elucidates their detailed morphologies, revealing that the brightest regions are concentrated at the peripheries of the quadrupolar structure (Fig. 2*a*). The partial elliptical ringlike structures in the equatorial region are different on the eastern and western sides of the nebula (labeled E1–E4). The E1 region is crossed by several arclike features. The radial extents of the equatorial and polar structures are similar, ranging from $6''$ – $7''$. There is a conspicuous lack of H_2 emission in the interior of the equatorial emission region, i.e., at radii of $\leq 4''$ as measured in the sky plane, except to the southeast, where the H_2 emission extends toward the center of the nebula in a very patchy manner.

The F165M image (Fig. 2*b*) shows the searchlight beam and multiple arc features reported by STWS98, in addition to the polar spindle structures. The bright inner regions of the spindles are distributed in a point-symmetric fashion about the nebular center. The equatorial emission seen at a very faint level is most likely due to emission in the $H_2 v = 1-0 S(9)$, $S(8)$, and $S(7)$ transitions (Hora & Latter 1994) that are present within the F165M filter bandpass. There is a compact blob just south of the southern tip of the northern spindle, which is not seen in the H_2 image. The images taken with the F187N, F190N, and F215N continuum filters look very similar to the F165M image (no $\text{Pa}\alpha$ emission was detected). Figure 2*c* shows the inner portion of the F606W WFPC2 image at the same spatial scale as the NICMOS images. The WFPC2 and F165M images were aligned with each other using the two stars visible in both images. We see that most of the bright arcs visible at high latitudes in the WFPC2 image can also be seen in the F165M image (the lower signal-to-noise ratio in the F165M image does not permit a comparison of the reflection nebulosities in these two images at latitudes $\leq 70^\circ$). The width of the dark lane as measured along the polar axis is smaller at $1.65 \mu\text{m}$ than at $0.6 \mu\text{m}$, presumably a result of the smaller extinction at the longer wavelength. The “shadow” region seen in the WFPC2 image in the southern lobe goes through the southern spindle and can be traced inward to within $2''.5$ of the expected position of the central star, indicating that the “plug” causing the shadow in the intersearchlight region lies closer to the star than $2''.5$, in a location that is obscured by the outer parts of the dust cocoon. In Figure 2*d* we have overlaid the $0.6 \mu\text{m}$ WFPC2 (blue) and the $H_2 S(1)$ (red) images. The fine structure in each image has been modestly enhanced. The brightest of the arclike features in the E1 region appears to be an extension of an arc seen faintly in the WFPC2 image.

TABLE 1
NICMOS OBSERVATIONS OF CRL 2688

Filter	T_{int}^a (s)	Reads ^b	$\phi_k^{c,d}$ (deg)	e_k^d	l_k^d	Comments
F165M	634	16	1.55–1.75 μm
F187N	895	20	$\text{Pa}\alpha$
F190N	1151	24	$\text{Pa}\alpha$ continuum
F212N	1215	25	$H_2 S(1) v = 1-0$
F215N	1215	25	H_2 continuum
POL0L	1215	25	8.8	0.7313	0.1552	1.9–2.1 μm
POL120L	1215	25	131.4	0.6288	0.2279	1.9–2.1 μm
POL240L	1215	25	248.2	0.8738	0.0673	1.9–2.1 μm

^a Combined exposure time of four dither positions.

^b Number of reads in the STEP16 MULTIACCUM sequence.

^c Polarizer angles measured from the NICMOS aperture offset angle of 224.5° , about the aperture center toward the +U3 axis.

^d From Hines et al. 1997.

We have made a detailed comparison of the distribution of the H_2 -emitting material, which is hot and shocked (see, e.g., Beckwith, Beck, & Gatley 1984; Hora & Latter 1994), and the more quiescent material seen in the scattered continuum from dust, free from wavelength-dependent extinction effects, by overlaying the H_2 line and F215N images (Fig. 3 [Pl. L46]). As expected (because both the dust column density and the incident starlight decrease with radius), the scattered $2 \mu\text{m}$ light, on the average, decreases in intensity with radius within the spindles. In conspicuous contrast, the H_2 emission peaks $5''$ – $7''$ away from the center. The compact blob seen at $1.65 \mu\text{m}$ in the dust cocoon region is seen more clearly in the $2.15 \mu\text{m}$ image. This blob, not seen in the WFPC2 images at $0.6 \mu\text{m}$, is clearly very red. The northern tip of the southern spindle can be seen jutting beyond the gently curving edge of the dust cocoon. This tip cannot be seen in the WFPC2 image, and only faintly so at $1.65 \mu\text{m}$ because of the higher extinction in the dust cocoon at shorter wavelengths. A detailed comparison of the brightness profiles of the two spindles will allow an estimate of the extinction toward this tip as a function of wavelength, which will be useful in constraining the physical properties of the dust cocoon.

3. ARCS, SPINDLES, AND THE DUST COCOON

Our F165M image shows that the brightness contrast of the arcs and the radial decrease of the scattered light are almost identical to those seen in the WFPC2 image by STWS98. This result implies that the extended nebula is optically thin to scattering in the 0.6 – $2 \mu\text{m}$ wavelength range, since the scattering efficiency is $Q_s \propto \lambda^{-4}$ for the small-sized grains that reside in the extended nebula (Jura, Balm, & Kahane 1995). Thus, in the following two results by STWS98, the lower limits (a result of not knowing whether the $0.6 \mu\text{m}$ scattering was optically thick or thin), can now be replaced by equalities: (1) the arcs represent enhancements in the mass-loss rate by factors at least as large as 2, and (2) the average mass-loss rate (or, less likely, the dust scattering efficiency) varies with radius at least as fast as $r^{-0.7}$.

The morphology of the polar spindles seen in the NICMOS images strongly supports the idea that they are bubbles resulting from the expansion of a collimated high-velocity outflow inside the AGB progenitor’s dense, slowly expanding (20 km s^{-1}) envelope. The high-velocity ($\approx 300 \text{ km s}^{-1}$) outflow is directly detected through CO millimeter-wave line observations (Young et al. 1992; Jaminet et al. 1992). The limb-brightened appearance of these bubbles results from the high-velocity wind

sweeping up the surrounding dense gas like a snowplow, creating hollow structures with thin dense walls. The linear extent of the polar spindles measured in both NICMOS and WFPC2 images indicates that this hydrodynamic interaction has been taking place for about 200 yr.

The origin of the equatorial H_2 emission is a puzzle, although the fact that its radial extent is almost identical to that of the polar spindles strongly suggests a common origin for the polar and equatorial structures. The H_2 emission spectrum implies that both the equatorial and polar H_2 emission arises in shocked gas (Beckwith et al. 1984; Hora & Latter 1994), indicating the presence of high-velocity gas in the equatorial region interacting with dense gas. The limb-brightened H_2 emission structures seen in the NICMOS images clearly confirm the shock hypothesis. Yet we see little or no H_2 emission in the radial region between the nebular center and the equatorial structures E1, E2, E3, and E4 (Fig. 2a), along the path presumably traversed by the high-velocity gas. One possibility is that the high-velocity gas flows out through channels between the northern and southern half of the dust cocoon surrounding the star—the channels are obscured from our view by the northern half of the dust cocoon, which is tilted toward us. A large $2\ \mu\text{m}$ extinction in the dust cocoon is not surprising, considering that the central star is not visible in the K -band images. The channels must be sufficiently nonrectilinear in order to prevent starlight from escaping and illuminating the equatorial region. Thus, the elliptical region lacking H_2 emission outlines the dense inner region of the dust cocoon obscuring the central star. The rather well-defined boundary of this region beyond which the equatorial H_2 emission manifests itself must then mark the transition of the $2\ \mu\text{m}$ extinction, $\tau_{\text{ext}}(2\ \mu\text{m})$, from $\gg 1$ to $\ll 1$. The radius of this boundary, which is presumably intrinsically circular but appears elliptical because it is seen nearly edge-on, is about $4''$. The minor-to-major axis ratio of the cocoon implies that its symmetry axis is inclined by 10° – 20° to the sky plane.

The searchlight beams seen in the WFPC2 image have been modeled by STWS98 as starlight escaping through annular polar cavities in the dust cocoon obscuring the central star and illuminating the surrounding nebula. Thus, the brightness variation across the searchlight beams is related simply to a latitudinal variation of radial optical depth in the dust cocoon around the central star ($\Delta\tau_{\text{cocoon}}$), which produces a latitudinal variation in the illumination of the nebular material. STWS98 find that $\Delta\tau_{\text{cocoon}}(0.6\ \mu\text{m}) \approx 2.3$, which implies, for small-sized grains, a $\Delta\tau_{\text{cocoon}}$ at near-IR wavelengths that is far too small to produce the searchlight-beam effect. We have used the STWS98 model to explicitly estimate $\Delta\tau_{\text{cocoon}}$ at $1.65\ \mu\text{m}$. If the optical depth at $1.65\ \mu\text{m}$ is a constant factor (say) h lower than that at $0.6\ \mu\text{m}$, then the illumination function (defined as the emergent intensity from the dust cocoon, normalized to be unity at its peak) is given by $I(1.65\ \mu\text{m}) = I(0.6\ \mu\text{m})^{(1/h)}$. Using $I(0.6\ \mu\text{m})$ given by STWS98 to estimate $I(1.65\ \mu\text{m})$, we find that $h \approx 1.6$ – 1.8 . Since, for amorphous grains of size $\leq 0.4\ \mu\text{m}$, the $1.65\ \mu\text{m}$ optical depth is a factor of 2.7 times smaller than at $0.6\ \mu\text{m}$ (Martin & Rogers 1987), the grains in the dust cocoon are certainly larger than $0.4\ \mu\text{m}$, and probably as large as $0.6\ \mu\text{m}$. The model provides a reasonable fit, but it is not as good as the fit at $0.6\ \mu\text{m}$ obtained by STWS98, especially in the “shadow” region, where the observed intensity is larger than in the model (Fig. 4). The poorer fit at $1.65\ \mu\text{m}$ is probably due to blending of scattered light with emission from dust at the high temperatures (1500–2000 K) expected for the H_2 line-emitting regions in the spindles (see § 4); Jones & Dyck (1978) estimate that thermal emission contributes $\approx 39\%$ of the $2\ \mu\text{m}$

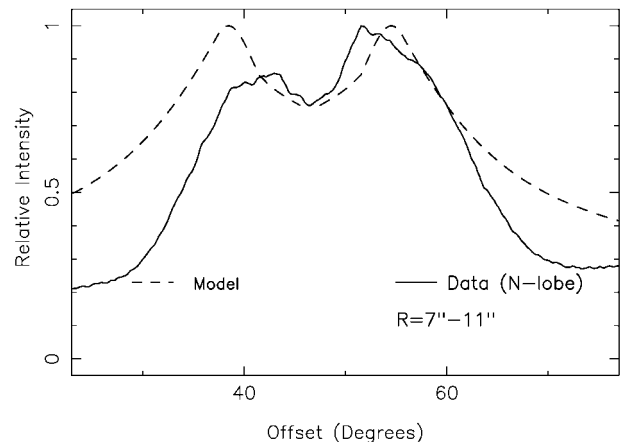


FIG. 4.—Observed and model $1.65\ \mu\text{m}$ intensity, integrated along the radius from $7''$ – $11''$, is shown as a function of angular offset for the northern lobe. The angular offset is measured from the horizontal axis of the images shown in Fig. 2b.

intensity in the northern spindle region. The blending of thermal emission with scattered light would tend to reduce the contrast across the searchlight beams, compared with that seen at a wavelength (like $0.6\ \mu\text{m}$) where we observe, almost exclusively, scattered light.

4. POLARIZATION

Figure 5 (Plate L47) presents the NICMOS camera 2 imaging polarimetry alongside ground-based data for comparison. Figure 6 (Plate L48) shows gray-scale images of the percentage polarization for the entire nebula and an enlarged view of the northern spindle. Each NICMOS polarizer has a different polarizing efficiency, and the relative polarizer position angles within the camera differ slightly from the nominal values of 0° , 120° , and 240° (Thompson et al. 1998). Therefore, a reduction algorithm different from that outlined in the NICMOS manual was used (Hines, Schmidt, & Lytle 1997). The observed signal from a polarized source of total intensity I and linear Stokes parameters Q and U measured through the k th polarizer oriented with a position angle (ϕ_k) is $S_k = A_k I + e_k (B_k Q + C_k U)$, where $A_k = \frac{1}{2} t_k (1 + l_k)$, $B_k = A_k \cos 2\phi_k$, $C_k = A_k \sin 2\phi_k$, e_k is the polarizing efficiency, t_k is the fraction of light transmitted for a 100% polarized input aligned with the polarizer’s axis (0.9667 for all polarizers), and l_k is the fraction transmitted (exclusive of that involved in t_k) with polarization perpendicular to the polarizer axis (see Table 1). After solving this system of equations to derive the Stokes parameters at each pixel, the percentage polarization (p) and position angle (θ) at that pixel were calculated in the standard way. A full error analysis that carries all of the uncertainties through the reduction process is still under development, but uncertainties of $\sigma_p \lesssim 5\%$ and $\sigma_\theta \lesssim 2^\circ$ are suggested by the variation in the polarization in regions of CRL 2688 where the structure appears fairly uniform (the instrumental polarization is $\leq 1\%$).

Overall, the NICMOS and ground-based polarimetry results agree quite well, once the NICMOS polarimetric images are binned to match the spatial resolution of the ground-based images. Both data sets show centrosymmetric patterns of position angle within the polar lobes, proving that the bipolar nebula is illuminated by a source hidden within the dark dust lane (Fig. 6). Note the departure from centrosymmetry in the dark lane region, where a system of aligned vectors appears. Such

patterns are frequently observed within the equatorial regions of bipolar reflection nebulae (see, e.g., Kastner & Weintraub 1995); the presence of such a pattern in CRL 2688 provides strong, independent evidence for the presence of a circumstellar disk. Other, more subtle, features of the polarization morphology of CRL 2688 that are seen in the ground-based polarization map—most notably, the east-west asymmetry of the region of aligned vectors—and the dissimilar polarization morphologies of the two polar lobes—are reproduced precisely in the NICMOS map, confirming that the NICMOS polarimetry is well calibrated. However, the superior resolution of the NICMOS data reveals polarization features that are not apparent in the ground-based polarization map. In particular, the NICMOS map shows that the degree of polarization is extremely high along some lines of sight through CRL 2688 (up to $\sim 80\%$ along some parts of the searchlight beams).

The spindles are highly polarized, especially near their outer edges where $p \approx 70\%–80\%$. The percentage polarization decreases in the interior in both spindles and is especially apparent in the northern spindle, where the polarization drops to $p \approx 50\%$ in some places. Although the polarizers' bandpass may admit as much as 10% of the H_2 emission, the reduced polarization occurs primarily in regions that do not emit significant H_2 (cf. Fig. 3). The decreased polarization within the spindles is probably caused by unpolarized emission from hot dust (see, e.g., Jones & Dyck 1978). The polarization is low ($p \sim 10\%$) in the equatorial H_2 regions, consistent with (a) their light being dominated by unpolarized line emission or (b) the polarization in these regions not resulting from scattering. One possibility, which merits further study, is that the polarization results from dichroic absorption of H_2 emission by aligned dust grains within the dark lane.

In § 2 we noted the presence of a compact, relatively red blob just south of the bottom of the northern spindle. This feature has low polarization ($p \approx 10\%–15\%$), demonstrating that it is self-luminous and not merely a compact region of scattered light. It appears somewhat extended and is far brighter than any field star in the K -band images, strongly suggesting that it is local to the dark lane and is neither a background nor a foreground object. The position angles of the high-polarization regions in the spindles and in the searchlight beams appear to rule out the blob as the primary illuminating source of the nebula. We conclude that the blob is most likely a secondary companion to the central post-AGB star at the core of the Egg Nebula. This secondary, located at a projected distance of ≈ 750 AU north of the central star, evidently has not significantly affected the centrosymmetric polarization pattern of the latter. Therefore, it is either significantly less luminous than the central star at $2 \mu\text{m}$ or, because of its location within the dust cocoon, its light cannot readily escape to illuminate the bipolar nebula. Note that the blob's fuzzy, nonstellar appearance also suggests that it is embedded in the dust cocoon. Our

3σ upper limit on a point source at the central star's expected position is 9.7×10^{-8} Jy at $1.65 \mu\text{m}$, which implies that the line-of-sight extinction optical depth to it is ≥ 18.5 at $1.65 \mu\text{m}$. The extinction toward the companion is unknown but is probably large, and hence we are unable to further constrain its properties.

5. SUMMARY

NICMOS has provided an unprecedented, high-resolution view of CRL 2688's optically obscured inner regions, offering a tantalizing glimpse of the detailed structure of the mysterious dust cocoon surrounding the central star. The emergence and evolution of bipolarity in a formerly spherical circumstellar envelope at the end of the AGB phase of stellar evolution is believed to be intimately connected with the formation, or preexistence, of a dusty cocoon that is concentrated toward the equatorial plane and with the interaction of a high-velocity collimated outflow with the progenitor AGB mass-loss envelope. The NICMOS images provide vivid, new evidence for the presence of both phenomena in CRL 2688. These images resolve the sharp interface between the high-velocity outflow that produces the polar spindles and the surrounding slow outflow that forms the extended nebula. The point-symmetric structure of the spindles suggests that the high-velocity outflow axis has changed with time. The dust cocoon also manifests itself clearly as a well-defined region of absorption in both H_2 and $1.65 \mu\text{m}$ images and as a region of aligned vectors in the NICMOS polarization map. Finally, examination of the images and polarization map yields the likely detection of a companion to the central post-AGB star in CRL 2688. The presence of this companion, which is apparently buried in the equatorial dust cocoon, may lend new weight to binary-based models (Morris 1990; Livio 1993; Soker & Livio 1994) of the structure of axisymmetric planetary nebulae in general and CRL 2688 in particular. However, the measured projected separation of 750 AU between the companion and the central star appears too large to provide direct support for these models or for the eccentric binary recently presented by Harpaz, Rappaport, & Soker (1997) to explain the complex morphology of the Egg Nebula.

We thank G. Schmidt and D. Lytle for their assistance with the polarimetry reduction and B. Stobie, L. Bergeron, and A. Evans for assistance with data calibration. R. S. and D. C. H. respectively acknowledge support from NASA grants NAS 7-1260 (WFPC2 project) and NAG 5-3042 (NICMOS project). J. H. K.'s research at MIT is supported in part by the Advanced X-Ray Astrophysics Facility Science Center as part of Smithsonian Astrophysical Observatory contract SVI-61010 under the NASA Marshall Space Flight Center.

REFERENCES

- Beckwith, S., Beck, S. C., & Gatley, I. 1984, *ApJ*, 280, 648
 Cox, P., et al. 1997, *A&A*, 321, 907
 Gatley, I., Depoy, D. L., & Fowler, A. M. 1988, *Science*, 242, 1264
 Jaminet, P. A., Danchi, W. C., Sandell, G., & Sutton, E. C. 1992, *ApJ*, 400, 535
 Jones, T. J., & Dyck, H. M. 1978, *ApJ*, 220, 159
 Jura, M., Balm, S. P., & Kahane, C. 1995, *ApJ*, 429, L33
 Harpaz, A., Rappaport, S., & Soker, N. 1997, *ApJ*, 487, 809
 Hines, D. C., Schmidt, G. D., & Lytle, D. 1997, in *The 1997 HST Calibration Workshop*, ed. S. Casertano et al. (Baltimore: STScI), in press
 Hora, J. L., & Latter, W. B. 1994, *ApJ*, 437, 281
 Kastner, J. H., Gatley, I., Merrill, K. M., Probst, R., & Weintraub, D. A. 1994, *ApJ*, 421, 600
 Kastner, J. H., & Weintraub, D. A. 1995, *AJ*, 109, 1211
 Knapp, G. R., Bowers, P. F., Young, K., & Phillips, T. G. 1994, *ApJ*, 429, L33
 Latter, W. B., Hora, J. L., Kelly, D. M., Deutsch, L. K., & Maloney, P. R. 1993, *AJ*, 106, 260
 Livio, M. 1993, in *IAU Symp. 155, Planetary Nebulae*, ed. R. Weinberger & A. Acker (Dordrecht: Kluwer), 279
 Martin, P. G., & Rogers, C. 1987, *ApJ*, 322, 374

- Morris, M. 1981, *ApJ*, 249, 572
- . 1990, in *From Miras to Planetary Nebulae: Which Path for Stellar Evolution?* ed. M. O. Mennessier & A. Omont (Gif-sur-Yvette: Frontières), 520
- Ney, E. P., Merrill, K. M., Becklin, E. E., Neugebauer, G., & Wynn-Williams, C. G. 1975, *ApJ*, 198, L129
- Sahai, R., et al. 1998, *ApJ*, in press (STWS98)
- Soker, N., & Livio, M. 1994, *ApJ*, 421, 219
- Thompson, R. I., Rieke, M., Schneider, G., Hines, D. C., & Corbin, M. R., 1998, *ApJ*, 492, L95
- Yamamura, I., Onaka, T., Kamijo, F., Deguchi, S., Ukita, N. 1995, *ApJ*, 439, L13
- Young, K., Serabyn, G., Phillips, T. G., Knapp, G. R., Gusten, R., & Schulz, A. 1992, *ApJ*, 385, 265
- Yusef-Zadeh, F., Morris, M., & White, R. L. 1984, *ApJ*, 278, 186

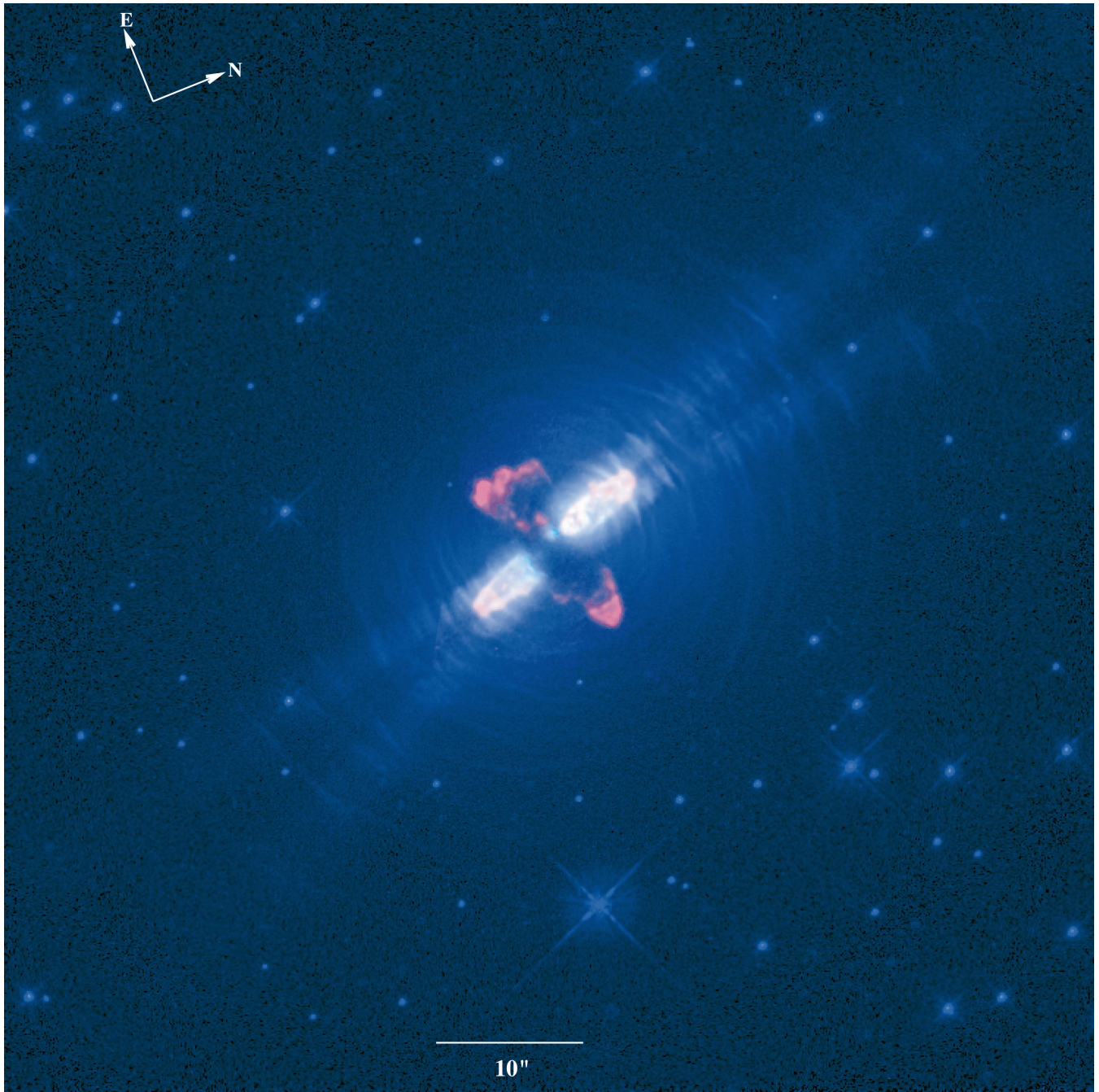
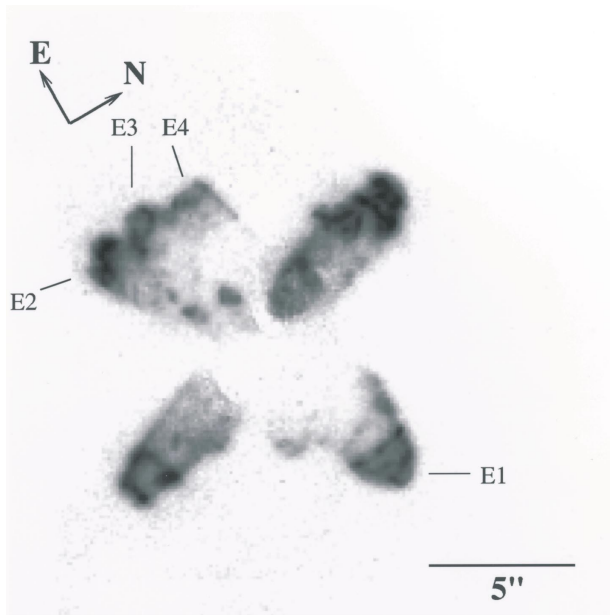
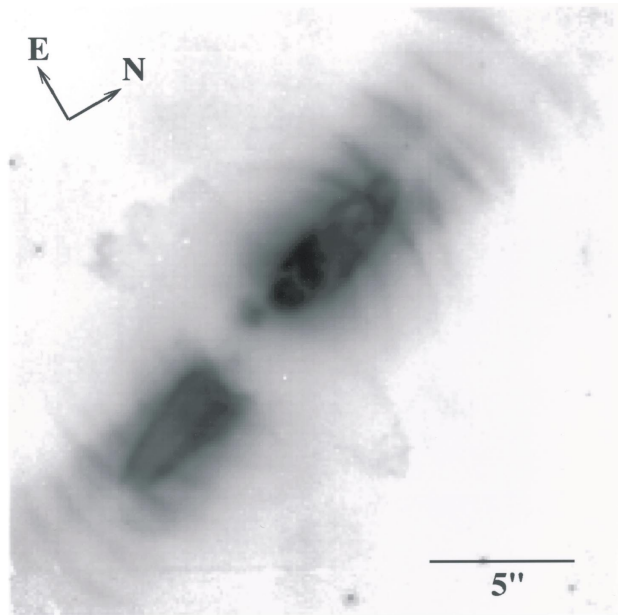


FIG. 1.—Composite color image of the protoplanetary nebula CRL 2688 showing the NICMOS continuum-subtracted $2.122\ \mu\text{m}$ $\text{H}_2\ S(1)$ image in red, the $1.65\ \mu\text{m}$ F165M image in green, and the WFPC2 $0.6\ \mu\text{m}$ image (from STWS98) in blue. The sharp structures in these images have been modestly enhanced.

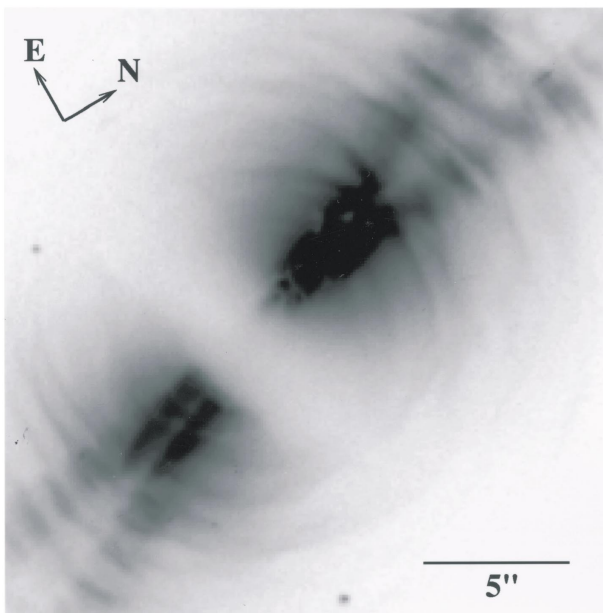
SAHAI et al. (see 492, L164)



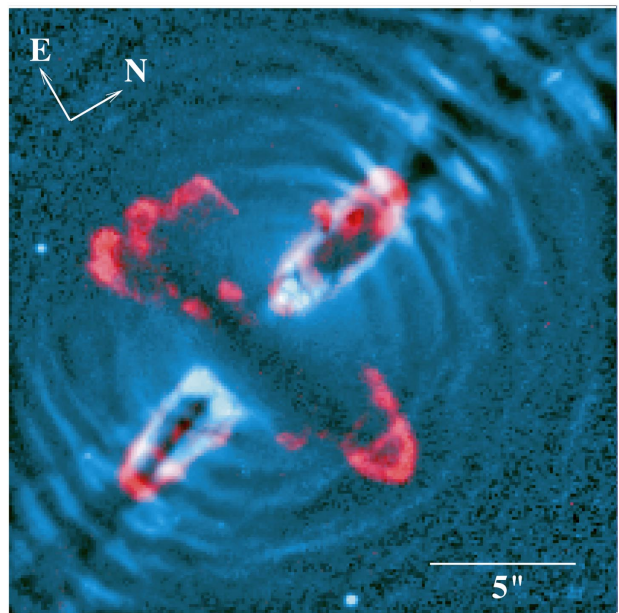
(a) 2.12 μm (H_2 $S(1)$ line)



(b) 1.65 μm (cont)



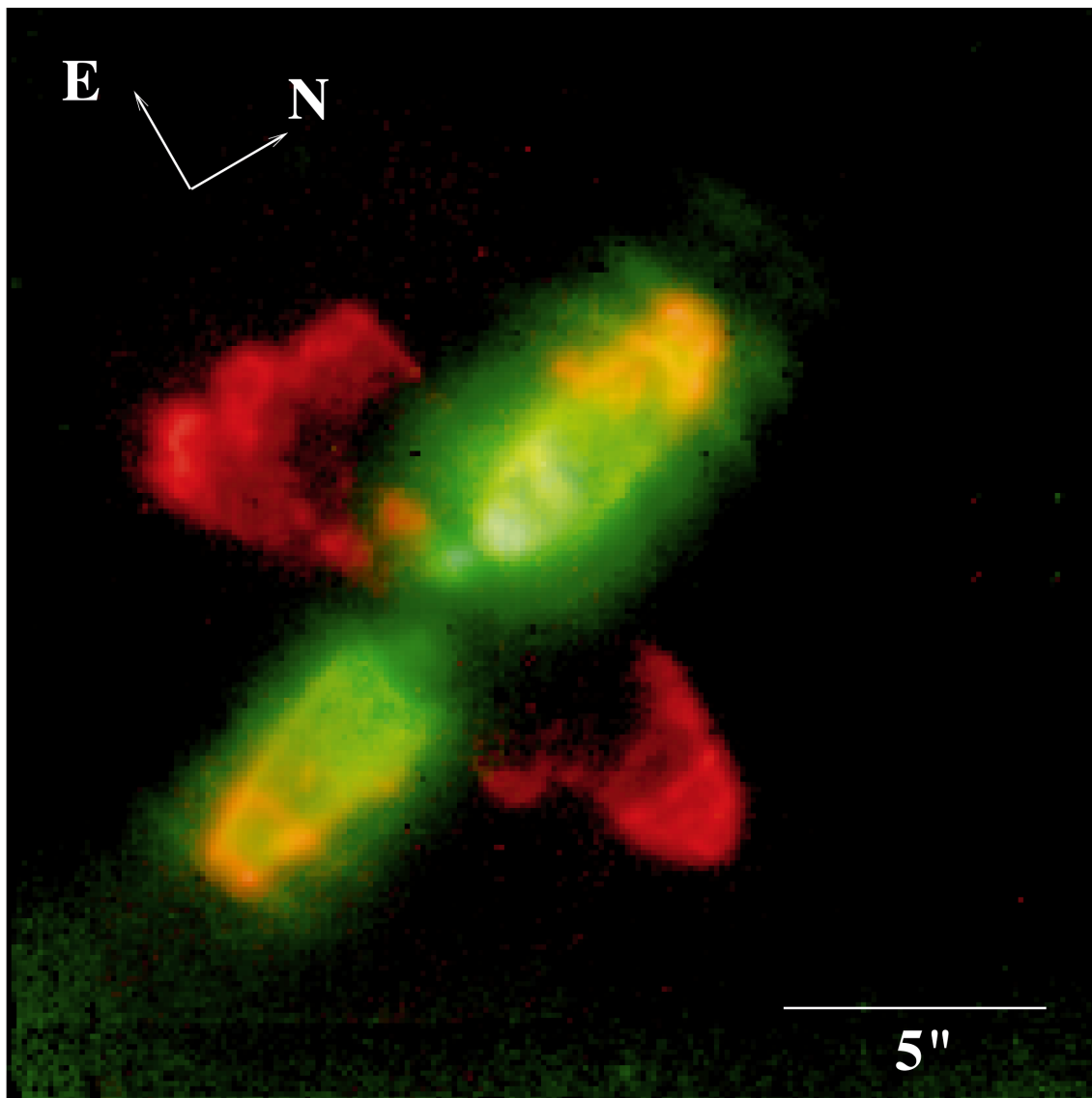
(c) 0.61 μm (cont)



(d) 0.61 μm (cont) & 2.12 μm (H_2 $S(1)$ line)

FIG. 2.—Near-infrared and optical images of the inner region of CRL 2688. NICMOS images in (a) H_2 $S(1)$ 2.122 μm line emission and (b) at 1.65 μm . (c) The same region of CRL 2688 taken from a WFPC2 image at 0.6 μm (STWS98). (d) Overlay of the 0.6 μm WFPC2 (blue-green) and the H_2 $S(1)$ (red) images. In (d), the fine structure has been enhanced in each image. An unsharp mask was generated from the logarithmic intensity image by replacing the intensity of each pixel by the 30th percentile value of all pixel intensities in a circular sample area with a 10 pixel radius, centered on that pixel; then a fraction of the unsharp mask was subtracted from the log image. A logarithmic stretch and reverse gray scale have been used in all images, and the maximum (black) and minimum (white) values of the intensity, respectively, are 1.2×10^{-13} and 2.3×10^{-15} $\text{ergs s}^{-1} \text{cm}^{-2} \text{arcsec}^{-2}$ in (a), 5.9×10^{-2} and 1.9×10^{-5} Jy arcsec^{-2} in (b), and 15.0 and 22.4 mag arcsec^{-2} in (c).

SAHAI et al. (see 492, L164)



2.15 μm (cont) & 2.12 μm (H_2 $S(1)$ line)

FIG. 3.— H_2 $S(1)$ line emission (*red*) and nearby 2.15 μm continuum intensity (*green*) in CRL 2688. A logarithmic stretch has been used for both images
SAHAI et al. (see 492, L164)

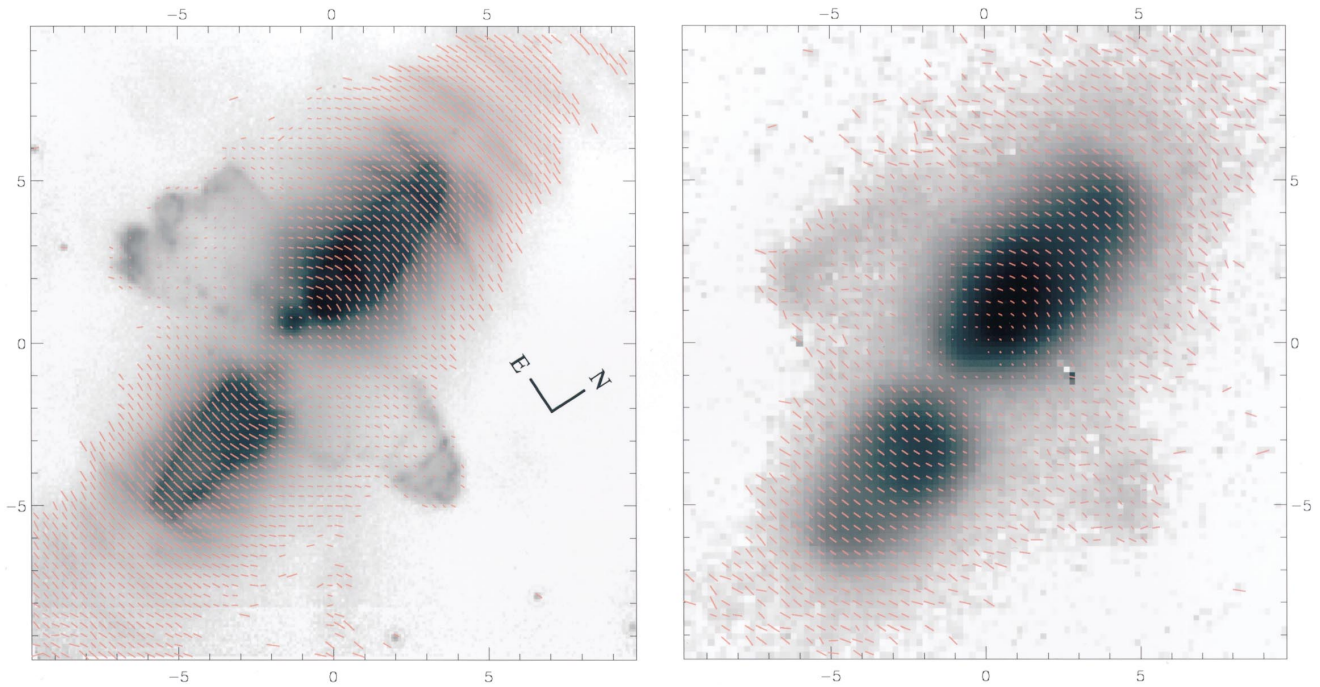


FIG. 5.—(a) NICMOS and (b) ground-based (*K*-band) polarimetric images of CRL 2688. The tick marks on both axes show offsets in arcseconds from the center. Orange lines indicate polarization and position angle (θ), with a maximum length of $p = 85\%$. Each inverse gray-scale image is the logarithm of the total intensity. The ground-based data were obtained in 1995 October with the 2.1 m telescope at KPNO, using the Cryogenic Optical Bench (COB) developed by NOAO (Kastner et al. 1994). The pixel scale was $0''.19$, and the seeing was $\sim 1''.5$. Vectors indicating the percentage polarization (length) and position angles are overplotted in all panels and represent the average value in 4×4 and 2×2 pixel bins in NICMOS and COB, respectively.

SAHAI et al. (see 492, L165)

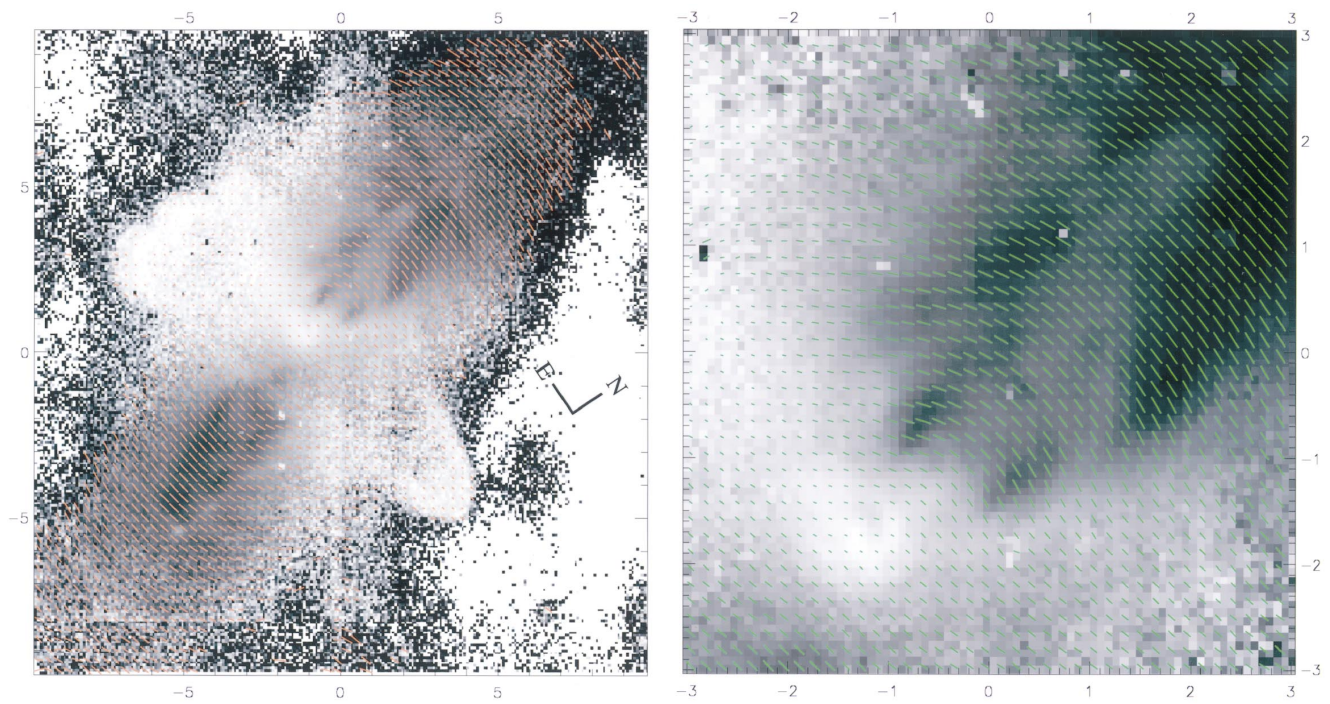


FIG. 6.—NICMOS polarimetric image of CRL 2688. The tick marks on both axes show offsets in arcseconds from the center. (a) The percentage polarization, p ; white = 0%, black = 100%. (b) Expanded view of the northern spindle and the blob. The green lines indicate the polarization and position angle (θ) plotted for 2×2 pixel bins, with a maximum length of $p = 75\%$.

SAHAI et al. (see 492, L165)